Title	Mechanistic study of C–H bond activation by O-2 on negatively charged Au clusters : alpha,beta-dehydrogenation of 1-methyl-4-piperidone by supported Au catalysts dagger
Author(s)	Miyazaki, Ray; Jin, Xiongjie; Yoshii, Daichi et al.
Citation	Catalysis science and technology, 11(10), 3333-3346 https://doi.org/10.1039/d1cy00178g
Issue Date	2021-03-21
Doc URL	https://hdl.handle.net/2115/84728
Type	journal article
File Information	20210317_MS-R1_Au-OMS-2_jh0322cleane.pdf

Mechanistic study of C–H bond activation by O_2 on negatively charged Au clusters: α,β-dehydrogenation of 1-methyl-4-piperidone by supported Au catalysts †

Ray Miyazaki, [1,‡] Xiongjie Jin,[2] Daichi Yoshii,[3] Takafumi Yatabe,[3] Tomohiro Yabe,[3] Noritaka Mizuno,[3] Kazuya Yamaguchi,[3,] and Jun-ya Hasegawa [1,*]*

[1]Institute for Catalysis, Hokkaido University, N21 W10 Kita-ku, Sapporo, Hokkaido 001-0021, Japan

[2]Department of Chemistry and Biotechnology, School of Engineering, The University of Tokyo, 7-3-1 Hongo, Bunkyo-ku, Tokyo 113-8656, Japan

[3]Department of Applied Chemistry, School of Engineering, The University of Tokyo, 7-3-1 Hongo, Bunkyo-ku, Tokyo 113-8656, Japan

‡**Present Address:** Fritz-Haber-Institut der Max-Planck-Gesellschaft, Faradayweg 4-6, D-14195 Berlin, Germany

ABSTRACT

Au nanoparticles supported on manganese oxide octahedral molecular sieve (OMS-2) can efficiently catalyze α,β-dehydrogenation of β-*N*-substituted saturated ketones using O_2 as the terminal oxidant. However, despite the utility of this reaction, the active sites and the reaction mechanism remain unclear. Here, the reaction mechanism for the Au/OMS-2-catalyzed aerobic α,β-dehydrogenation of 1-methyl-4-piperidone was investigated mainly by using density functional theory (DFT) calculations. From control experiments under various reaction conditions, we found that O_2 plays an important role in the α,β-dehydrogenation over Au nanoparticles. Thus, we attempted to clarify the mechanism for the α,β-dehydrogenation of 1-methyl-4-piperidone on Au nanoparticle catalysts by DFT calculations using Au cluster models. The reaction was found to cleave the $C–H^\alpha$ and $C–H^\beta$ bonds in that order. An O_2 molecule adsorbed on the negatively charged Au cluster caused by charge transfer from OMS-2 was found to be sufficiently activated to abstract the H^α atom in the 1-methyl-4-piperidone substrate. This indirect H^α abstraction by the activated O_2 was energetically more favorable than direct H^α abstraction by the Au cluster. The subsequent H^β abstraction was found to be promoted by adsorbed oxygen species (i.e., HOO, OH, and O) formed after the H^α abstraction. The reaction mechanism proposed in this study provides general insight into the aerobic C–H bond activation by supported Au catalysts.

1. Introduction

Enaminones, β-*N*-substituted α,β-unsaturated ketones, are very important synthetic intermediates for fine chemical and pharmaceutical production.[1-4] Selective α,β-dehydrogenation of β-*N*-substituted saturated ketones is one of the most effective reactions for synthesizing enaminones, and several efficient homogeneous catalysts have been developed for this reaction using various oxidants.[5, 6] However, to achieve more environmentally friendly dehydrogenation, heterogeneous catalytic systems using O_2 as the terminal oxidant should be developed. With regard to heterogeneous systems, supported Pd-based nanoparticles have been reported to show high catalytic performance for the aerobic dehydrogenation of cyclohexanone derivatives to the corresponding cyclohexenones or phenols.[7-9] Recently, our research group discovered the specific dehydrogenation ability of Au nanoparticle catalysts and achieved, for the first time, the widely applicable dehydrogenation of β-heteroatom-substituted saturated ketones to the corresponding unsaturated ketones, including enaminones, using O_2 as the terminal oxidant.[10] For example, in the presence of Au nanoparticles supported on manganese oxide octahedral molecular sieve OMS-2 (hereafter denoted Au/OMS-2), the α,β-dehydrogenation of 1-methyl-4-piperidone efficiently proceeded under mild conditions (50 °C under an air atmosphere), selectively affording the desired enaminone in an almost quantitative yield (Scheme 1).[10]

Scheme 1. Reaction scheme of α,β-dehydrogenation of 1-methyl-4-piperidone by the Au/OMS-2 catalyst.[10]
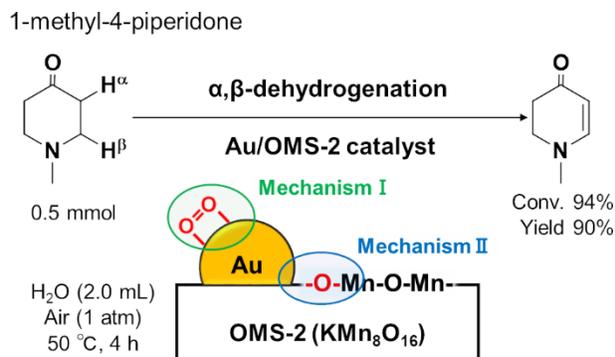
Because both O_2 and the OMS-2 support are potential oxidants, two reaction mechanisms are expected: a reaction at the Au surface with O_2 as an oxidant (mechanism I in Scheme 1) and that at the perimeter region between Au and the lattice oxygen (mechanism II in Scheme 1). Indeed, the α,β-dehydrogenation of 1-methyl-4-piperidone using Au/OMS-2 even proceeded under an Ar atmosphere (i.e., without O_2). Further, X-ray diffraction (XRD) analysis revealed that the OMS-2 support is completely reduced to Mn_3O_4 after the reaction under an Ar atmosphere.[10] This result suggests a reaction mechanism occurring in the perimeter region that proceeds with lattice oxygen consumption (mechanism II in Scheme 1). On the other hand, in the case of carbon-supported Au nanoparticle catalysts (Au/C) that have no lattice oxygen, the α,β-dehydrogenation also proceeded efficiently under an O_2 atmosphere but does not proceed at all under an Ar atmosphere (see Section 3.1 and S8 in the Electronic Supplementary Information (ESI)). This result suggests that not only mechanism II but also the mechanism at the Au surface using O_2 (mechanism I in Scheme 1) could co-occur during Au/OMS-2-catalyzed dehydrogenation. However, the details of these reaction mechanisms remain largely unexplored. In particular, even the role of O_2 is unknown with respect

to mechanism I. Additionally, information about mechanism I would give general insights into the aerobic C–H bond activation mechanism that is independent of the support material and, thus, would open a way for the design of high-performance catalysts. Therefore, we focus here on the α,β-dehydrogenation mechanism of 1-methyl-4-piperidone at the Au surface using O_2 (mechanism I in Scheme 1).

Because it is very difficult to elucidate the origin of specific catalytic effects and determine the reaction mechanisms of supported Au catalysts experimentally, a theoretical approach is essential. To date, several theoretical studies to elucidate the mechanism of Au-catalyzed C–H bond activation for several reactions (e.g., alcohol oxidation) using Au cluster models have been reported, and two types of reaction mechanisms have been proposed: (i) direct C–H bond activation by Au and (ii) indirect C–H activation by O_2 or O atoms adsorbed on the Au surface.[11-15] Additionally, it should be noted that the charge state of the Au clusters can be controlled by the choice of the support material or polymer ligands, and this is an important factor affecting the catalytic activity.[14-23] In particular, the relationship between O_2 activation and the charge state of Au clusters has been reported in previous theoretical studies,[24-27] and this would affect indirect C–H bond activation by O_2. Thus, to elucidate the C–H bond activation mechanism of supported Au catalysts, the effect of the charge state of Au clusters should be investigated. However, there is still no detailed (plausible or theoretical) explanation for the aforementioned relationship.

Thus, in this study, the mechanism of the α,β-dehydrogenation of 1-methyl-4-piperidone over supported Au nanoparticle catalysts was examined mainly by density functional theory (DFT) calculations using Au cluster models. The aim of these calculations was to understand the general aerobic Au-catalyzed C–H bond activation mechanism. Additionally, we investigated the relationship between the C–H bond activation mechanism and the charge state of the Au cluster

affected by the support or H_2O (solvent). In this paper, we first explain the results of several control experiments for the Au-catalyzed α,β-dehydrogenation of 1-methyl-4-piperidone (Section 3.1). After a discussion of the electronic structure of the Au cluster on the OMS-2 support and adsorbed O_2 (Section 3.2), the reaction mechanism of the first C–H$^\alpha$ bond cleavage step is proposed, and the key role of the charge state of the Au cluster is also illustrated (Section 3.3). Then, the origin of the activity of the adsorbed O_2 is clarified in relation to the charge state of the Au cluster (Section 3.4), and the reaction mechanism for the second C–H$^\beta$ bond cleavage step (Section 3.5) and the total catalytic cycle are also discussed (Section 3.6). Concluding remarks are given in the last section.

2. Computational Details

2.1 Au$_{10}$/OMS-2 Model

To investigate the electronic structure of the Au cluster on the OMS-2 support, an Au$_{10}$ cluster on a surface slab model of OMS-2 (Au$_{10}$/OMS-2 model: Figure 1a) was constructed with periodic boundary conditions.
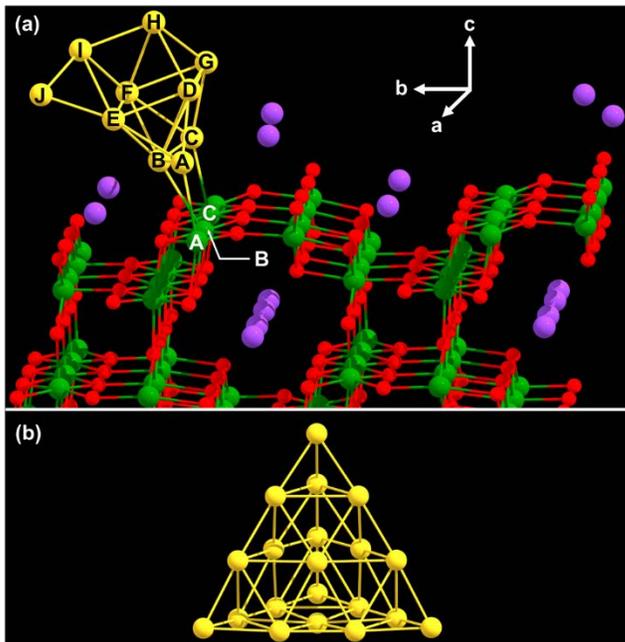
Figure 1. (a) Au_{10}/OMS-2 model. (b) Au_{20} model. Red: oxygen, green: manganese, purple: potassium, yellow: gold.

Tompsett and Islam et al. reported that the (100) surface is the most stable surface of α-MnO$_2$ (i.e., OMS-2 without K atoms) in their previous theoretical calculations.[28] Our calculations also showed that the surface energy of the (100) surface of OMS-2 is more stable than that of the (110) surface (the next stable surface of α-MnO$_2$)[28] by 0.07 J/m^2. Therefore, the (100) surface was adopted for the computational model of the OMS-2 surface in this study. The (100) surface of OMS-2 was modeled using a (4 $\times$ 2) unit cell with 25-layers ($K_{40}Mn_{128}O_{256}$: Figure S1 in the ESI). The lattice constant of this slab was set to $a = 11.5$ Å, $b = c = 19.6$ Å, and $\alpha = \beta = \gamma = 90$ °, which were determined by cell optimization of the bulk structure of OMS-2. The calculated lattice constants of bulk OMS-2 was in good agreement with the experimental value ($a = 11.4$ Å, $b = c = 19.6$ Å (these are the multiplied values for (4 $\times$ 2) super cell)).[29] Each slab was separated by a 25-Å vacuum layer perpendicular to the (100) surface.

K atoms are located at the hollow sites of the (100) surface if the (100) surface is simply cut from the bulk structure, as shown in Figure S1a (8-hollow structure). However, once half of the K atoms are moved to the terrace sites from the hollow sites, the surface structure (4-hollow_4-terrace structure, Figure S1b) is more stable than the original structure by 47.1 kcal/mol. Additionally, the 4-hollow_4-terrace structure is more stable than other surface structures (more details are given in Section S1 in the ESI). Therefore, the 4-hollow_4-terrace structure was adopted in the present study. Furthermore, the Au_{10} model could be adsorbed only on the terrace site of the OMS-2 surface because other adsorption sites were occupied by K atoms in the 4-hollow_4-teracce structure. According to these procedures, the Au_{10}/OMS-2 model (Figure 1a) was constructed to investigate the electronic structure of the Au cluster on the OMS-2 surface.

Calculations using the Au_{10}/OMS-2 model were carried out using spin-polarized DFT calculations with the FHI-aims code (version: 171221).[30] The Perdew−Burke−Ernzerhof (PBE) functional[31] was used as the exchange–correlation functional. The numerical atom-centered orbital (NAO) basis set[30] with the default "light" settings were used for geometry optimization, and single-point energy calculations of optimized structures were performed with the default "tight" settings (although the confinement radius for K atoms was changed to 4.0 Å). In addition, atomic-scaled zeroth-order regular approximation (Atomic ZORA)[30] was adopted to incorporate the relativistic effects. A Γ-centered grid of $18 \times 6 \times 6$ k-points was used for the cell optimization of the bulk OMS-2 structure, and a Γ-centered grid of $5 \times 3 \times 1$ k-points were used for the slab models. The bottom 11 layers of OMS-2 were fixed to the bulk structure during geometry optimization. The initial spin state of OMS-2 was obtained from previous theoretical calculations by Cockayne and co-workers.[32]

The Au$_{10}$/OMS-2 model was compared with the Au$_5$/OMS-2 model, and the two models gave similar results for the electronic structures of the Au cluster and the adsorbed O$_2$ (see more details in Section S10 in ESI). The model dependence is expected to be not so significant.

2.2 Au$_{20}$ Model

In the present study, we focused on the α,β-dehydrogenation mechanism of 1-methyl-4-piperidone at the Au surface, in which the lattice oxygen of the OMS-2 support is not directly involved. Thus, the Au$_{20}$ model (cluster model, Figure 1b) was adopted to investigate the reaction mechanism of the Au-catalyzed aerobic α,β-dehydrogenation of 1-methyl-4-piperidone. Because a previous study[33] showed that the tetrahedral pyramidal structure is the most stable conformation of Au$_{20}$, we also adopted pyramidal structures in the present study. The total charge of the Au$_{20}$ model was changed to incorporate the effect from the support material or H$_2$O (see Section 3.3), and three types of Au$_{20}$ models were constructed: Au$_{20}^{0\pm}$, Au$_{20}^{1-}$, and Au$_{20}^{2-}$.

The Au$_{20}$ models were compared with Au$_{10}$ models for the O$_2$ adsorption and C−H activation. As shown in Section S10 in ESI, the two models gave similar results for the calculated charges, O−O distance, adsorption energy, and reaction energy for the C−H cleavage. The model dependence is expected to be not so significant.

DFT calculations were performed for the Au$_{20}$ model using Gaussian 09.[34] The M06 functional[35] was used for the exchange–correlation functional. The Stuttgart/Dresden basis set with effective core potential[36] was employed for Au, and the 6-31G(d, p) basis sets[37] were used for the other elements. The ultrafine grid (99 590 grid) was used for the integration grid of numerical integration. All reactants, products, and transition state structures were connected by intrinsic reaction coordinate (IRC) calculations. Additionally, normal mode analysis was performed, and we

confirmed that each of the equilibrium and transition states contained zero and one imaginary frequency, respectively.

The result by the M06 functional with Gaussian 09 code was compared with that obtained by the PBE functional with the FHI-aims code. With the $Au_{20}^{0\pm}$, Au_{20}^{1-}, and Au_{20}^{2-} models, the structures and charges on the adsorbed O_2 were compared because these values are related to the O_2 activation. As the result given in Section S5 of ESI, the structures and charges obtained with the two computational settings are similar to each other.

3. Results and Discussion

3.1 Dehydrogenation of 1-Methyl-4-piperidone under Various Conditions

As mentioned in the introduction, the reaction mechanism at the Au surface (mechanism I in Scheme 1) and that involving the lattice oxygen in the perimeter region (mechanism II in Scheme 1) could both occur during Au/OMS-2-catalyzed α,β-dehydrogenation under an air atmosphere. To investigate these reaction mechanisms, the initial reaction rates of the α,β-dehydrogenation of 1-methyl-4-piperidone were measured in the presence of Au/Al$_2$O$_3$ or Au/OMS-2 at different partial pressures of O_2. As shown in Figures S8 and S9, the initial reaction rate of the Au/Al$_2$O$_3$-catalyzed reaction was dependent on the partial pressure of O_2, and the reaction hardly proceeded in the absence of O_2 (i.e., an Ar atmosphere). On the other hand, when Au/OMS-2 was used, the reaction proceeded even under an Ar atmosphere, suggesting that OMS-2 itself acted as the terminal oxidant (see Figure S8). Moreover, the initial reaction rate of the Au/OMS-2-catalyzed reaction was also dependent on the partial pressure of O_2, similar to that of the Au/Al$_2$O$_3$-catalyzed

reaction (see Figure S9). Thus, this O_2 pressure dependence indicates the presence of a catalytic process on the Au surface with O_2 consumption in which OMS-2 is not directly involved.

We investigated more details of the reaction mechanism without the involvement of the lattice oxygen of the metal oxide supports using an Au/C catalyst. The α,β-dehydrogenation of 1-methyl-4-piperidone by the Au/C catalyst proceeded only in the presence of O_2 (see entries 1 and 2 in Table S4). These results indicate that the reaction can proceed only on the Au surface by utilizing O_2 and that the lattice oxygen of metal oxides is not necessarily required for α,β-dehydrogenation.

3.2 Electronic Structures of the Au Cluster and Adsorbed O_2 Species on Au/OMS-2

In this section, the electronic structure of the Au cluster on OMS-2 is discussed based on the results of DFT calculations using the Au_{10}/OMS-2 model (Figure 1a). Additionally, the adsorption structures of O_2 on the Au_{10}/OMS-2 model are also discussed. As shown below, the Au cluster on the OMS-2 support is negatively charged as a result of charge transfer from OMS-2. Furthermore, the adsorbed O_2 is activated to form a superoxide state by charge transfer from the Au cluster on OMS-2.

3.2.1 Electronic Structure of the Au Cluster on the OMS-2 Support

Hirshfeld charge analysis[38] was performed for the Au_{10}/OMS-2 model to analyze the atomic charges of each Au atom. As shown in Table 1, the total charge of the Au_{10} cluster in the Au_{10}/OMS-2 model was calculated to be −0.42. The negative charges are distributed over the Au atoms in the second and third layers (i.e., Au^D–Au^J except for Au^E).

Table 1. Hirshfeld charge of each Au atom.[a]

Layer	Hirshfeld Charge			
1	Au^A	Au^B	Au^C	
	0.00	0.13	0.02	
2	Au^D	Au^E	Au^F	Au^G
	−0.06	0.01	−0.06	−0.13
3	Au^H	Au^I	Au^J	
	−0.09	−0.09	−0.15	
Total	Au_{10}			
	−0.42			

[a]Indexes of Au atoms correspond to those in Figure 1a.

To investigate the reorganization of the electronic structure, the electron density difference, $\Delta\rho(Au_{10}/OMS\text{-}2)$, was calculated using eq (1). This reorganization is induced by the interaction between the Au_{10} cluster and the OMS-2 support.

$$\Delta\rho(Au_{10}/OMS\text{-}2) = \rho(Au_{10}/OMS\text{-}2) - \rho(Au_{10}) - \rho(OMS\text{-}2) \tag{1}$$

Here, $\rho(model\ name)$ is the total electron density of each model. $\rho(Au_{10})$ and $\rho(OMS\text{-}2)$ were independently obtained by single-point calculations. The atomic coordinates were taken from those of the $Au_{10}/OMS\text{-}2$ model. As shown in Figure 2, the electron density increases in the Au_{10} region. In particular, the electron density increases around the Au–Mn bonds and Au atoms in the second and third layers of the Au_{10} cluster. This result is consistent with the result of the Hirshfeld charge analysis (cf. Table 1). On the other hand, the electron density decreases around the Mn and O atoms of the OMS-2 surface. These results indicate the formation of Au–Mn bonds and charge transfer from OMS-2 to the Au cluster. On the other hand, the changes in the electron density around the K atoms on the surface can be interpreted as the polarization of the charge density. The Hirshfeld charges of K atoms did not show any meaningful change after the Au_{10} cluster was attached to the OMS-2 model.
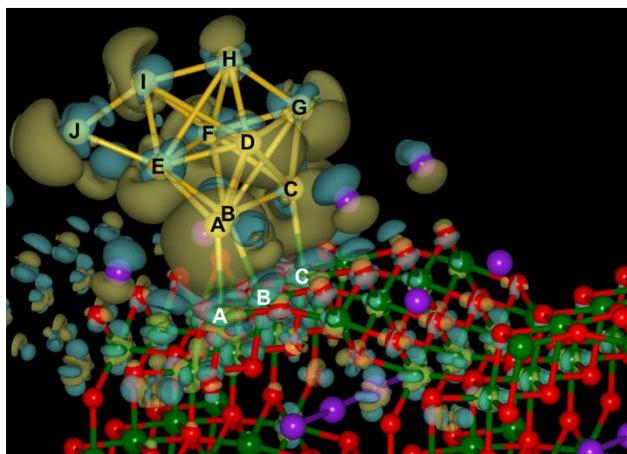
Figure 2. Electron density difference in the Au_{10}/OMS-2 model. The dark yellow isosurface indicates electron accumulation and the blue isosurface indicates electron depletion. Isosurface value is 0.01 $Å^{-3}$. Red: oxygen, green: manganese, purple: potassium, yellow: gold.

The density of states (DOS) of the Au_{10}/OMS-2 model was also calculated (Figure 3). We focused on the DOS projected onto all Au atoms and three Mn atoms bonded to the Au cluster (i.e., Mn^A, Mn^B, and Mn^C in Figure 1a) because the electron density difference analysis (cf. Figure 2) suggested that the interaction between Mn and Au is important for charge transfer. The results of DOS analysis for the Au_{10}/OMS-2 model are shown in Figure 3b. Around the valence and near the Fermi level, the energy levels of Au and Mn overlapped well (indicated by red arrows in Figure 3b), indicating the formation of Au–Mn bonds. The same DOS analysis was performed for an isolated OMS-2 model (OMS-2 without Au_{10}) and an isolated Au_{10} model (Au_{10} without OMS-2) (see Figures 3a and 3c, respectively). In the isolated Au_{10} model, unfilled bands were observed above the Fermi level (indicated by red arrows in Figure 3c). In contrast, they were shifted below the Fermi level in the Au_{10}/OMS-2 model (indicated by red arrows in Figure 3b), which is likely due to the interaction between Au and Mn. The valence band of the Mn atoms of the isolated OMS-

2 model (indicated by the red arrow in Figure 3a) is also shifted to the lower energy region in the Au$_{10}$/OMS-2 model (indicated by red arrows in Figure 3b). These results also suggested that valence electrons around the OMS-2 surface were transferred to the Au cluster to form Au–Mn bonds.
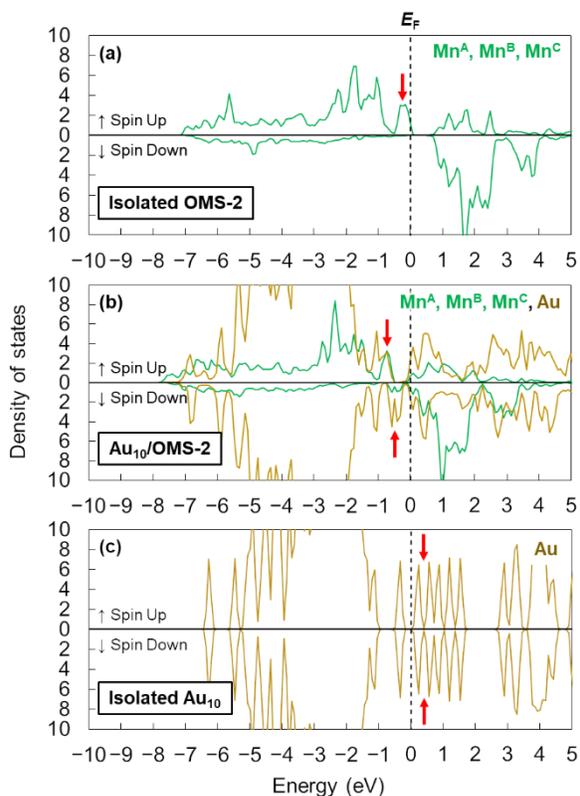

Figure 3. Atom projected DOS of (a) the isolated OMS-2 model, (b) the Au$_{10}$/OMS-2 model, (c) the isolated Au$_{10}$ model. Green line: Sum of the total DOS projected to Mn atoms bonded to Au atoms (indexes of Mn atoms correspond to those in Figure 1a). Yellow line: Sum of the total DOS projected to Au atoms. The Fermi energy (E_F) was set to 0.0 eV.

3.2.2 Electronic Structure of Adsorbed O$_2$ on the Au$_{10}$/OMS-2 Model

14

As mentioned in Section 3.1, when using Au/C, the α,β-dehydrogenation of 1-methyl-4-piperidone hardly proceeded in the absence of O_2 (see Table S4). Additionally, the rate of reaction on the Au surface without the involvement of lattice oxygen of OMS-2 showed a roughly first-order dependence on the O_2 partial pressure in Au/OMS-2 (cf. Figure S9). Therefore, O_2 is an essential factor for the catalytic cycle at the Au surface. Thus, the adsorption structures and electronic states of O_2 on the Au_{10}/OMS-2 model were investigated.

In the Au_{10} cluster, the most negatively charged adsorption site (Ads-site I) was the bridge site between Au^I and Au^J (cf. Figure 1a and Table 1). In contrast, one of the most positively charged adsorption site (Ads-site II) was a bridge site between Au^B and Au^E (cf. Figure 1a and Table 1). These two sites having opposite characteristics were selected to evaluate the O_2 adsorption capability. Although the bridge site between Au^B and Au^C was more positively charged than Ads-site II, that site was ruled out because there is not sufficient space for O_2 adsorption. The perimeter region between Au and OMS-2 was not investigated because we focused on the catalysis at the Au surface in which the lattice oxygen or its vacancy of the OMS-2 support are not directly involved (Mechanism I in Scheme 1). However, in other supported Au catalysts (e.g., Au/TiO_2 catalyst[39-43]), the perimeter site plays a key role in O_2 activation.

The adsorption structures of O_2 on the two adsorption sites are shown in Figure 4. In the case of Ads-site II, a large structural change in the Au_{10} cluster occurred during geometry optimization. As a result, the O^B atom changed its binding site from Au^E to Au^I. In this discussion, the bridge site between Au^B and Au^I is called Ads-site II* (Figure 4b). The adsorption energies for Ads-sites I and II* were calculated to be −33.6 and −4.8 kcal/mol, respectively. The results indicate that O_2 could be adsorbed on both Ads-site I and II* but is preferentially adsorbed on the more negatively charged sites. As shown in Figure 4, the O–O bond distances of adsorbed O_2 are 1.43 and 1.41 Å

on Ads-site I and Ads-site II*, respectively, which are longer than that in gas phase (1.22 Å). In addition, the adsorbed O_2 is negatively charged by more than -0.40 (Table 2). These results suggest that adsorbed O_2 is in a superoxide state and is activated because of charge transfer from the negatively charged Au cluster to the π^* orbital of O_2. As discussed in the next section, the C–H^α bond of 1-methyl-4-piperidone is cleaved by activated O_2 with a reasonable activation energy.
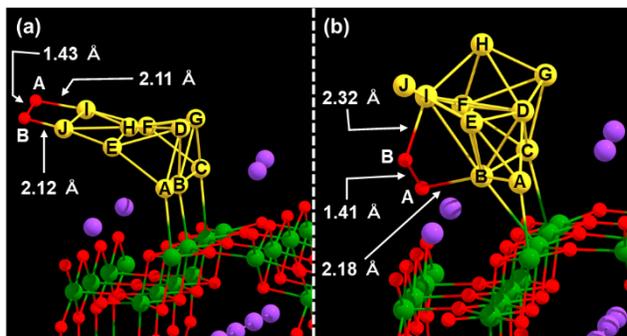

Figure 4. Adsorption structures of O_2 on (a) Ads-site I and (b) Ads-site II*. Red: oxygen, green: manganese, purple: potassium, yellow: gold.

Table 2. Hirshfeld charge of Au atoms and adsorbed O_2.[a]

	Ads-site I	Ads-site II*
O^A	–0.23	–0.18
O^B	–0.23	–0.22
Au^A	–0.02	0.03
Au^B	0.07	0.15
Au^C	–0.02	0.01
Au^D	–0.06	–0.04
Au^E	–0.08	–0.03
Au^F	–0.08	–0.05
Au^G	–0.06	–0.15
Au^H	0.01	–0.07
Au^I	0.00	0.00
Au^J	0.00	–0.18
$Au_{10} + O_2$	–0.70	–0.73

[a] For the indexes of the O and Au atoms, see Figure 4.

3.3 First C–H Bond Cleavage Step

In this section, the first C–H bond cleavage step of 1-methyl-4-piperidone is described using the Au_{20} model (Figure 1b). As mentioned above, our calculations showed that OMS-2 can donate electrons to Au and that O_2 can be activated on the negatively charged Au. In addition, we also obtained several experimental results suggesting that electron donation to Au is important even when electron-donating OMS-2 supports are not used. For example, we found that the Au/C-catalyzed aerobic dehydrogenation of 1-methyl-4-piperidone hardly proceeds when using toluene

17

as the solvent but efficiently proceeds in H_2O (Table S4, entries 1 and 3). A previous theoretical study showed that a negatively charged Au cluster is formed by charge transfer from adsorbed H_2O.[44] Our calculations also show that the charge transfer from adsorbed H_2O to the Au_{20} model occurs by -0.09 per H_2O molecule. Therefore, it can be considered that the Au/C-catalyzed reaction proceeds in H_2O because the adsorbed H_2O causes Au to become negatively charged. From the above-mentioned calculations and experimental results, we focused on the relationship between the catalytic activity for C–H bond activation and the negative charge state of the Au cluster. Thus, the positively charged Au cluster model was ruled out, and we constructed three Au_{20} models having negative charge states (± 0, -1, and -2) for detailed investigation: $Au_{20}{}^{0\pm}$, $Au_{20}{}^{1-}$, and $Au_{20}{}^{2-}$.

Using these three models, two types of C–H bond activation pathways (Scheme 2) were investigated. In the direct C–H bond activation pathway (Scheme 2a), the C–H bond of 1-methyl-4-piperidone is directly activated by Au. In the indirect C–H bond activation pathway (Scheme 2b), an adsorbed O_2 molecule is involved in hydrogen abstraction from 1-methyl-4-piperidone. We note that the calculated activation energies for O_2 dissociation were more than 40 kcal/mol in all Au_{20} models. On the basis of this result, the atomic O species from adsorbed O_2 can be eliminated as possible active species for the first indirect C–H activation. As discussed below, the indirect pathway is energetically favorable and is the main reaction pathway of the first C–H bond cleavage step.

Scheme 2. (a) Direct and (b) indirect pathways for the first C–H bond cleavage step.

(a) Direct C–H bond activation pathway

(b) Indirect C–H bond activation pathway by adsorbed O_2
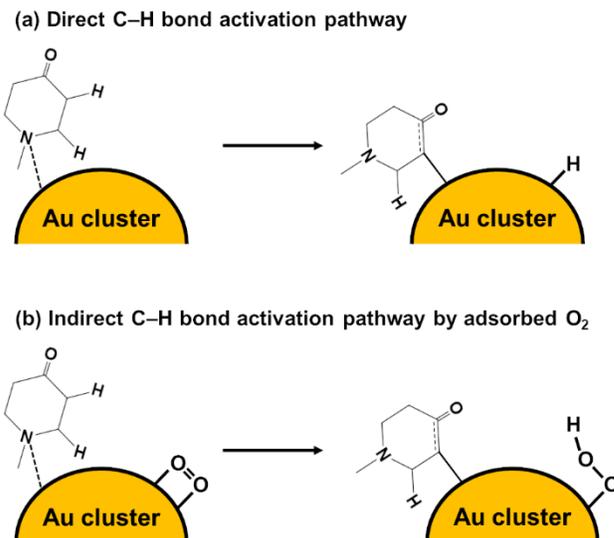
3.3.1 Direct C–H Bond Activation Pathway

First, the direct C–H bond activation pathway was investigated using the Au_{20} models. To obtain the structure of the reactant state, several adsorption sites of 1-methyl-4-piperidone were investigated for each charge state of the Au cluster. Of these, the most stable adsorption structure of the reactant molecule was selected (more details are given in Section S2 in the ESI). From these reactant states, all possible direct C–H bond activation pathways were investigated. Below, we discuss the reaction pathways having the lowest activation energies of the possible pathways. Additionally, both C–H$^\alpha$ and C–H$^\beta$ bonds (cf. Scheme 1) were tested for the first C–H bond cleavage step.

Potential energy diagrams of the direct C–H$^\alpha$ bond activation pathways for each model are shown as broken lines in Figure 5. The optimized structures along the reaction pathways are also shown in Figure 6. As shown in Figure 5, the activation energies of the direct pathways were more

than 40 kcal/mol in all models (E_{aA1} = 54.2 kcal/mol for the $Au_{20}^{0\pm}$ model, E_{aB1} = 44.8 kcal/mol for the Au_{20}^{1-} model, and E_{aC1} = 44.7 kcal/mol for the Au_{20}^{2-} model). Furthermore, regardless of the charge state, these elementary processes were calculated to be endothermic. The product states (A2, B2, and C2 in Figures 5 and 6) are more unstable than the reactant states (A1, B1, and C1 in Figure 5 and 6) by 44.2, 41.9, and 18.7 kcal/mol, respectively.

The direct C–H$^\beta$ bond activation pathways were also investigated (see more details in Section S4 in the ESI). As shown in Figure S3, the direct C–H$^\beta$ activation pathways were also endothermic reactions, having large activation energies (> 40 kcal/mol). In summary, direct C–H bond activation is not kinetically or thermodynamically favorable, and the charge state of the Au cluster does not change the endothermicity or reduce the high activation barrier of this pathway.
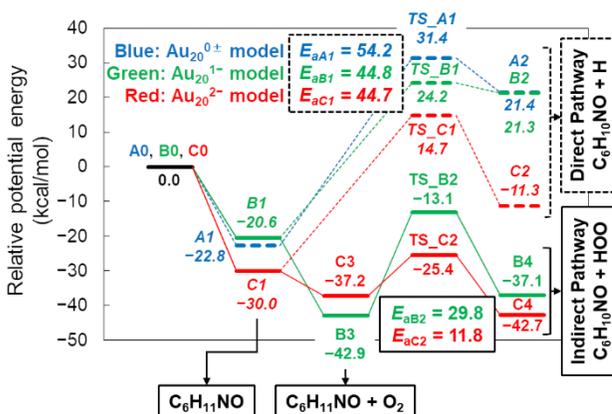

Figure 5. Potential energy diagram of the C–H$^\alpha$ bond activation at the first C–H bond cleavage step. Broken lines are direct C–H$^\alpha$ bond activation pathways, and solid lines are indirect C–H$^\alpha$ bond activation pathways. Energies of A0, B0, and C0 states are defined as the sum of the energies of the isolated species: $Au_{20}^{0\pm}$, O_2, and 1-methyl-4-piperidone for A0; Au_{20}^{1-}, O_2, and 1-methyl-4-piperidone for B0 and Au_{20}^{2-}, O_2, and 1-methyl-4-piperidone for C0.
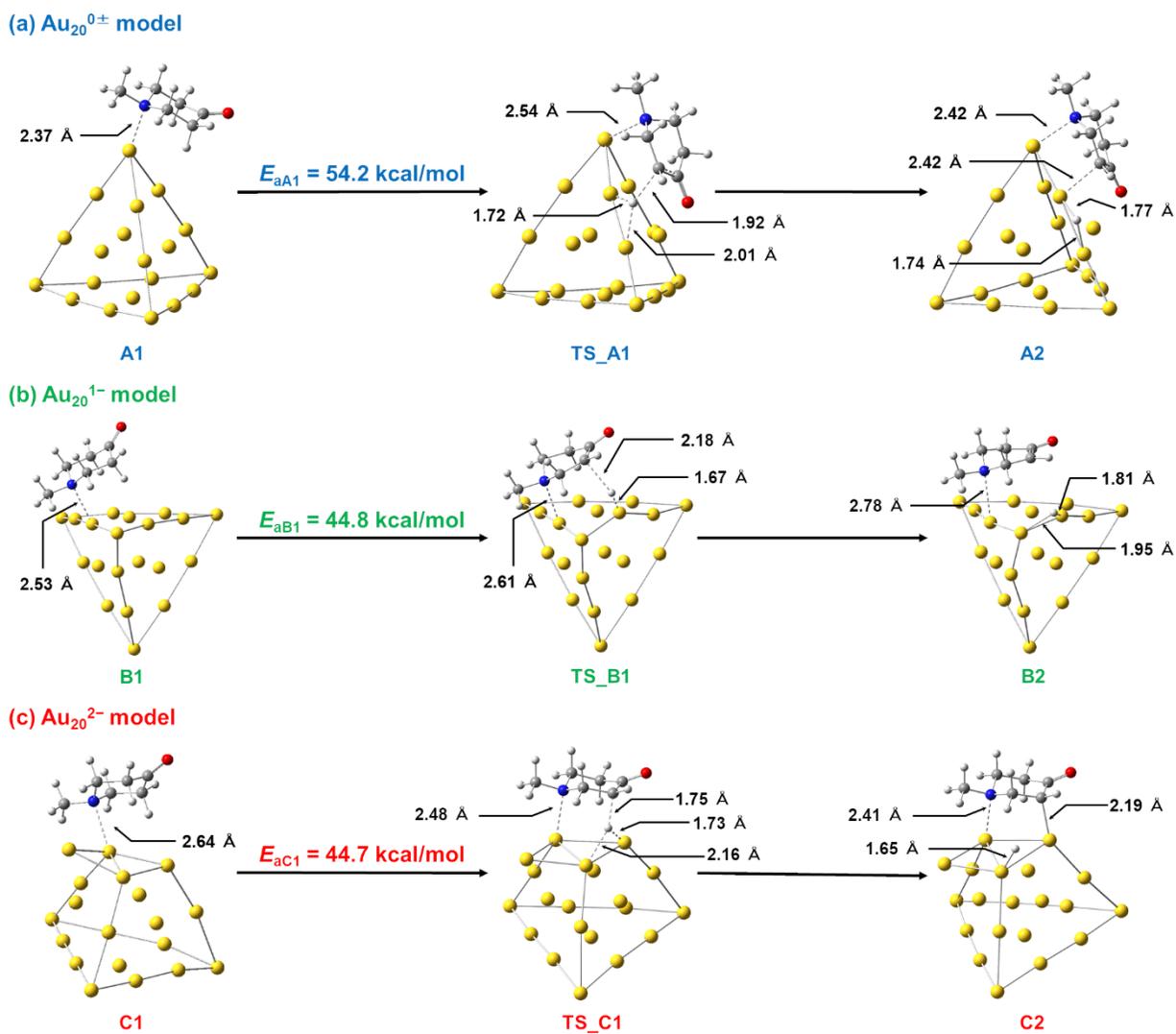
Figure 6. Optimized structures of the reactant, product and transition states of direct C–H$^\alpha$ bond activation on the (a) $Au_{20}{}^{0\pm}$, (b) $Au_{20}{}^{1-}$, and (c) $Au_{20}{}^{2-}$ models. Red: oxygen, blue: nitrogen, gray: carbon, white: hydrogen, yellow: gold.

3.3.2 Indirect C–H Bond Activation Pathway

In this pathway, the adsorbed O_2 first abstracts the H$^\alpha$ or H$^\beta$ atom of 1-methyl-4-piperidone (Scheme 2b). To begin with, the adsorption structures of O_2 on the Au_{20} model were investigated

following the method of a previous study for the Au_{20}^{1-} cluster.[11] In the present study, O_2 adsorption on the $Au_{20}^{0\pm}$ and Au_{20}^{2-} models was also considered. For the spin multiplicity, the $Au_{20}^{0\pm}$ and Au_{20}^{2-} models with O_2 were calculated as the singlet state, and the Au_{20}^{1-} model with O_2 was calculated as the doublet state (see more details in Section S3 in the ESI). The BR1 site (see the adsorption site of O_2 of B3 and C3 in Figure 7) is the most stable adsorption site in both the Au_{20}^{1-} and Au_{20}^{2-} models, and the calculated adsorption energies are −21.1 and −12.5 kcal/mol in the Au_{20}^{1-} and Au_{20}^{2-} models, respectively. On the other hand, O_2 adsorption on the $Au_{20}^{0\pm}$ model was calculated to be endothermic (cf. E_{ads} in Table S2), indicating that no stable O_2 adsorption was expected in the $Au_{20}^{0\pm}$ model. From these results, the indirect C–H activation pathway was investigated using the Au_{20}^{1-} and Au_{20}^{2-} models. This choice is also supported by the results obtained using the Au_{10}/OMS-2 model, in which the Au cluster plus O_2 is negatively charged, as discussed in Section 3.2.

For subsequent calculations, the BR1 site was selected as the O_2 adsorption site in the reactant state, and 1-methyl-4-piperidone was co-adsorbed on the neighboring adsorption sites of the BR1 site. Using these structures, all possible indirect C–H$^\alpha$ and C–H$^\beta$ activation pathways were investigated. The potential energy diagrams of the indirect C–H$^\alpha$ bond activation pathways for each model are shown as solid lines in Figure 5. The reaction pathways having the lowest activation energies are shown in this diagram. The optimized structures along the indirect reaction pathways are also shown in Figure 7. As shown in Figure 5, the activation energies of this reaction pathway are less than 30 kcal/mol in both models (E_{aB2} = 29.8 kcal/mol with the Au_{20}^{1-} model and E_{aC2} = 11.8 kcal/mol with the Au_{20}^{2-} model). These values are smaller than those of the direct C–H bond activation pathway by more than 15 kcal/mol. Furthermore, the product state is considerably stabilized. In the Au_{20}^{1-} model, reaction energy E_r (energy difference between

22

reactant state (E[R]) and product state (E[P]): $E_r = E[P] - E[R]$) of the indirect pathway is only +5.8 kcal/mol, indicating the large endothermicity in the direct pathway ($E_r = +41.9$ kcal/mol) was significantly reduced. In particular, the indirect pathway in the Au_{20}^{2-} model turned to an exothermic reaction ($E_r = -5.5$ kcal/mol), although the direct pathway is endothermic ($E_r = +18.7$ kcal/mol).

Additionally, indirect $C–H^\beta$ bond activation pathway was also investigated. As shown in Figure S3, the calculated activation energies of indirect $C–H^\beta$ bond cleavage are higher than those of indirect $C–H^\alpha$ bond cleavage by 5.8 kcal/mol in the Au_{20}^{1-} model and 15.1 kcal/mol in the Au_{20}^{2-} model. The difference in the activation barrier between the $C–H^\alpha$ and $C–H^\beta$ cases can be explained by the stability of the intermediate. After H abstraction, the substrate becomes negatively charged, and the intermediate formed by α-deprotonation of 1-methyl-4-piperidone is 36.1 kcal/mol more stable than that formed in the case of β-deprotonation in the gas phase because the acidity of H^α is greater than that of H^β. These results suggest that indirect $C–H^\alpha$ bond activation by adsorbed O_2 on the negatively charged Au clusters is an energetically favorable pathway. Additionally, the activation energy is reduced when the Au cluster is more negatively charged.
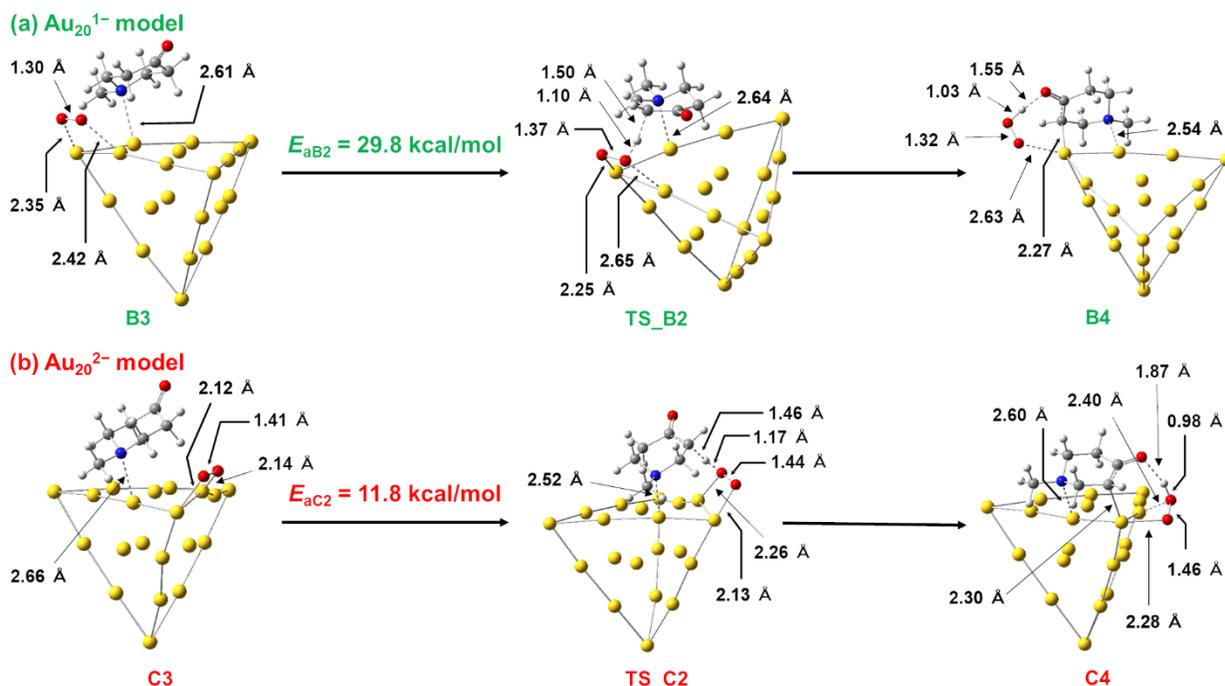
Figure 7. Optimized structures of the reactant, product, and transition states for indirect C–H$^{\alpha}$ bond activation on the (a) Au_{20}^{1-} and (b) Au_{20}^{2-} models. Red: oxygen, blue: nitrogen, gray: carbon, white: hydrogen, yellow: gold.

3.4 Electronic Structure of O_2 on the Au Cluster

O_2 activation by the Au cluster is key to the indirect C–H$^{\alpha}$ bond activation mechanism. To understand the relationship between the charge state of the Au cluster and O_2 activation, the electronic structure of the adsorbed O_2 was analyzed for each Au_{20} charge state. As discussed below, O_2 becomes a superoxide and is well activated for hydrogen abstraction because of the charge transfer from the Au cluster.

The highest occupied molecular orbitals (HOMOs) of the most stable adsorption structures of O_2 on each Au_{20} model (cf. Section S3) are shown in Figure 8. The HOMO is delocalized over

24

both the Au_{20} clusters and O_2 moieties in the $Au_{20}^{0\pm}$ and Au_{20}^{1-} models, and the HOMO involves the π^* orbital of the O_2 molecule. In the Au_{20}^{2-} model, the HOMO is localized on the O_2 moiety, and the π^* character becomes clearer. As shown in Figure 8 and Table 3, the O–O bond distance increased and the negative charge on O_2 increased when a more negatively charged model was used. These results indicate that O_2 is in a superoxide state and is well activated on the negatively charged Au_{20} cluster models owing to the charge transfer from the Au cluster to the π^* orbital of O_2.
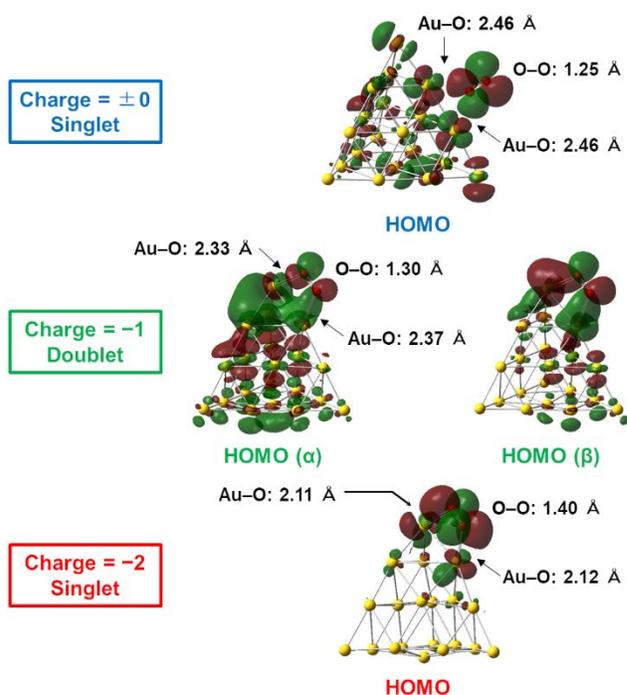

Figure 8. HOMO of the adsorbed O_2 on Au_{20} models. Isosurface value is 0.02 $Å^{-3}$. Red: oxygen, yellow: gold.

Table 3. Charge of O_2 adsorbed on the Au_{20} models.

	$Au_{20}^{0\pm}$ Model	Au_{20}^{1-} Model	Au_{20}^{2-} Model	Au_{10}/OMS-2 Model (Ads-site I)
NPA Charge of O_2	−0.27	−0.54	−0.95	−
Hirshfeld Charge of O_2	−0.31	−0.50	−0.78	−0.46

Furthermore, the electronic structure of adsorbed O_2 on the Au_{20} model was compared with that on the Au_{10}/OMS-2 model. Although the computational code and DFT functional are different, common trends were observed in these two models (for more details, see Section S5 in the ESI). The sum of the Hirshfeld charge of the Au_{10} cluster plus O_2 was calculated to be −0.70 when O_2 was adsorbed on Ads-site I of the Au_{10}/OMS-2 model (cf. Table 2), and the charge on O_2 was −0.46. In the Au_{20}^{1-} model, the natural population analysis (NPA) and Hirshfeld charges of the adsorbed O_2 are −0.54 and −0.50, respectively (Table 3). Additionally, the O–O and Au–O bond distances of O_2 on Ads-site I are similar to those in the Au_{20}^{2-} model (cf. Figures 4a and 8). In particular, the O–O bond lengths in the Au_{10}/OMS-2 model and that in the Au_{20}^{2-} model are 1.43 and 1.40 Å, respectively. From these results, both the charge state and structure of O_2 on the negatively charged Au_{20} models are similar to those on the Au_{10}/OMS-2 model.

Next, the isolated Au_{20} and isolated O_2 were compared. The energy levels of the HOMO, the singly occupied molecular orbital (SOMO), and the lowest unoccupied molecular orbital (LUMO) are shown in Figure 9. The HOMO and SOMO levels of the isolated Au_{20} models increase as the total charge becomes more negative. The HOMO level of the $Au_{20}^{0\pm}$ model is lower than the LUMO level of O_2. On the other hand, the HOMO levels of the Au_{20}^{1-} and Au_{20}^{2-} models are higher than the LUMO level of the isolated O_2. These results indicate that electron transfer from

Au to O_2 can occur more easily in the more negatively charged Au_{20} cluster. This is one possible reason why O_2 is well activated in the negatively charged Au_{20} models. However, the HOMO level of the Au_{20}^{2-} model is positive, which means that the −2 charge state results in an unstable electronic structure. Thus, the Au_{20}^{2-} model may not exist in reality. In contrast, the Fermi energy of the Au_{10}/OMS-2 model was calculated to be −4.71 eV, indicating that the negatively charged Au cluster in the Au_{10}/OMS-2 model is stable.
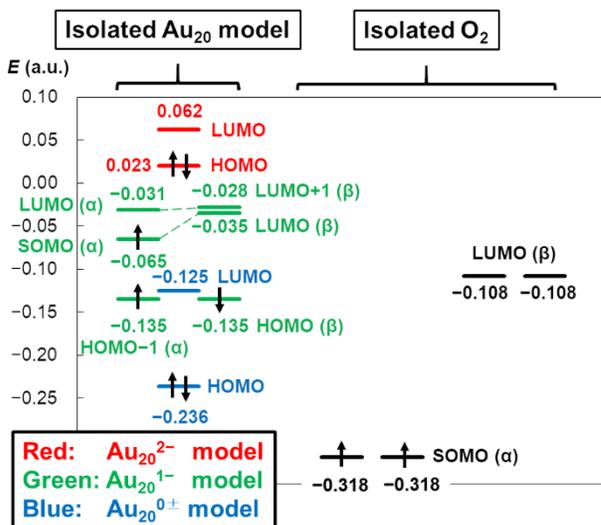

Figure 9. Orbital energy diagram of isolated Au_{20} models and O_2.

The above-mentioned electronic structure also affects the hydrogen affinity of adsorbed O_2 (HA_{O2}), as shown by Eq. (2).

$$HA_{O2} = [E(\text{AuHOO}) − (E(\text{AuO}_2) + E(\text{H}))] \tag{2}$$

Here, $E(\text{AuHOO})$ and $E(\text{AuO}_2)$ are the potential energies of the adsorbed states of HOO and O_2 on the Au_{20} model, respectively, and $E(\text{H})$ is the potential energy of an isolated hydrogen atom. HA_{O2} was calculated using the Au_{20}^{1-} and Au_{20}^{2-} models. The initial structures for geometry optimization of each structure were taken from the product states of the indirect C–H^α activation

pathway. HA_{O2} of the Au_{20}^{1-} and Au_{20}^{2-} models were calculated to be -75.3 and -86.9 kcal/mol, respectively, indicating that the interaction between hydrogen atom and adsorbed O_2 is stronger in the more negatively charged system. This result can be explained by the degree of O_2 activation, as discussed above, and this is one possible reason why the -2 charge state results in the lowest activation energy for the indirect pathway. Additionally, the hydrogen affinity of the isolated O_2^- anion was calculated to be -61.0 kcal/mol. This value is smaller than those of the adsorbed cases, which suggests that the interaction with Au enhances the hydrogen abstraction capability of the adsorbed O_2.

3.5 Second C–H Bond Cleavage Step for Enaminone Formation

After the first C–H$^\alpha$ bond cleavage by the adsorbed O_2, there are five possible C–H$^\beta$ bond activation pathways to generate the corresponding enaminone, as shown in Scheme 3. Specifically, these are the (a) direct pathway, in which the C–H$^\beta$ bond is directly activated by Au, (b) HOOH generation pathway, in which the C–H$^\beta$ bond is activated by adsorbed HOO species generated by the indirect C–H$^\alpha$ bond activation, (c) H_2O generation pathway, in which the H$^\beta$ is abstracted by the OH species generated by O–O bond cleavage of the HOO species, (d) OH generation pathway, in which H$^\beta$ is abstracted by the O species generated by O–O bond cleavage of the HOO species, and (e) HOO generation pathway, in which the C–H$^\beta$ bond is activated by the adsorbed O_2. Because the total charge of the Au cluster plus adsorbed O_2 is close to -1.0 in the Au_{10}/OMS-2 model (cf. Table 2), we focus on the reaction mechanism with the Au_{20}^{1-} model in this section. As shown below, the (b) HOOH generation pathway, (c) H_2O generation pathway, and (d) OH generation pathway are plausible routes for the C–H$^\beta$ bond cleavage step.

Scheme 3. Five possible reaction pathways in the second C–H$^{\beta}$ bond cleavage step.
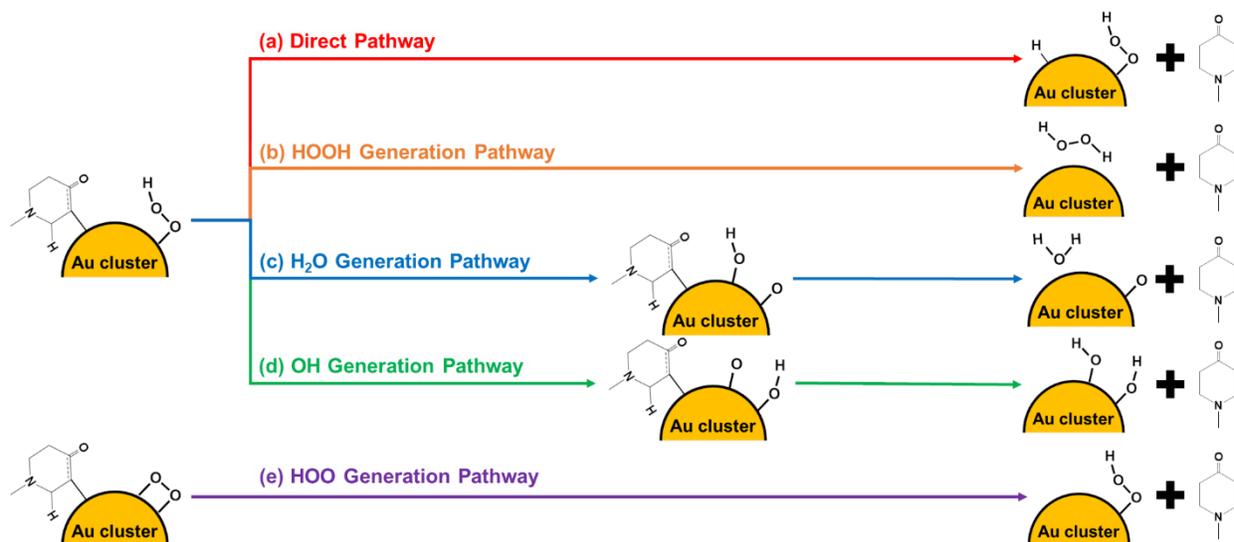
Potential energy diagrams of the C–H$^{\beta}$ activation pathways with the Au$_{20}{}^{1-}$ model are shown in Figure 10, and the optimized structures along the reaction pathways are shown in Figure 11. In the direct and HOOH generation pathways, the conformations of the adsorbed species changed from those in B4 (product state of the C–H$^{\alpha}$ activation step) to reactive conformations (Figure 11: B7 and B9, respectively) before C–H$^{\beta}$ bond activation. Although these conformational changes are necessary for the H$^{\beta}$ atom to interact with Au atoms or HOO species, the resulting conformations are more unstable than B4 by 10.7 and 7.2 kcal/mol, respectively. In this model, we could find no other stable conformations that are connected to low-lying transition states than those shown in Figure 11. The transition states of the direct and HOOH generation pathways are 23.6 and 14.3 kcal/mol above B7 and B9, respectively.
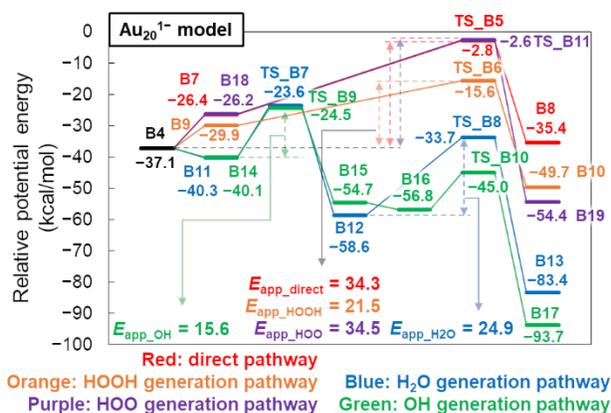
Figure 10. Potential energy diagram of the second C–H$^\beta$ bond cleavage step with the Au$_{20}^{1-}$ model: (a) direct pathway (red line), (b) HOOH generation pathway (orange line), (c) H$_2$O generation pathway (blue line), (d) OH generation pathway (green line), and (e) HOO generation pathway (purple line). In this figure, the potential energies are relative to the sum of the energies of the isolated species, i.e., Au$_{20}^{1-}$, O$_2$, 1-methyl-4-piperidone, and adsorbed state of O$_2$ on the Au$_{20}^{1-}$ model (for more details, see Section S6 in the ESI).
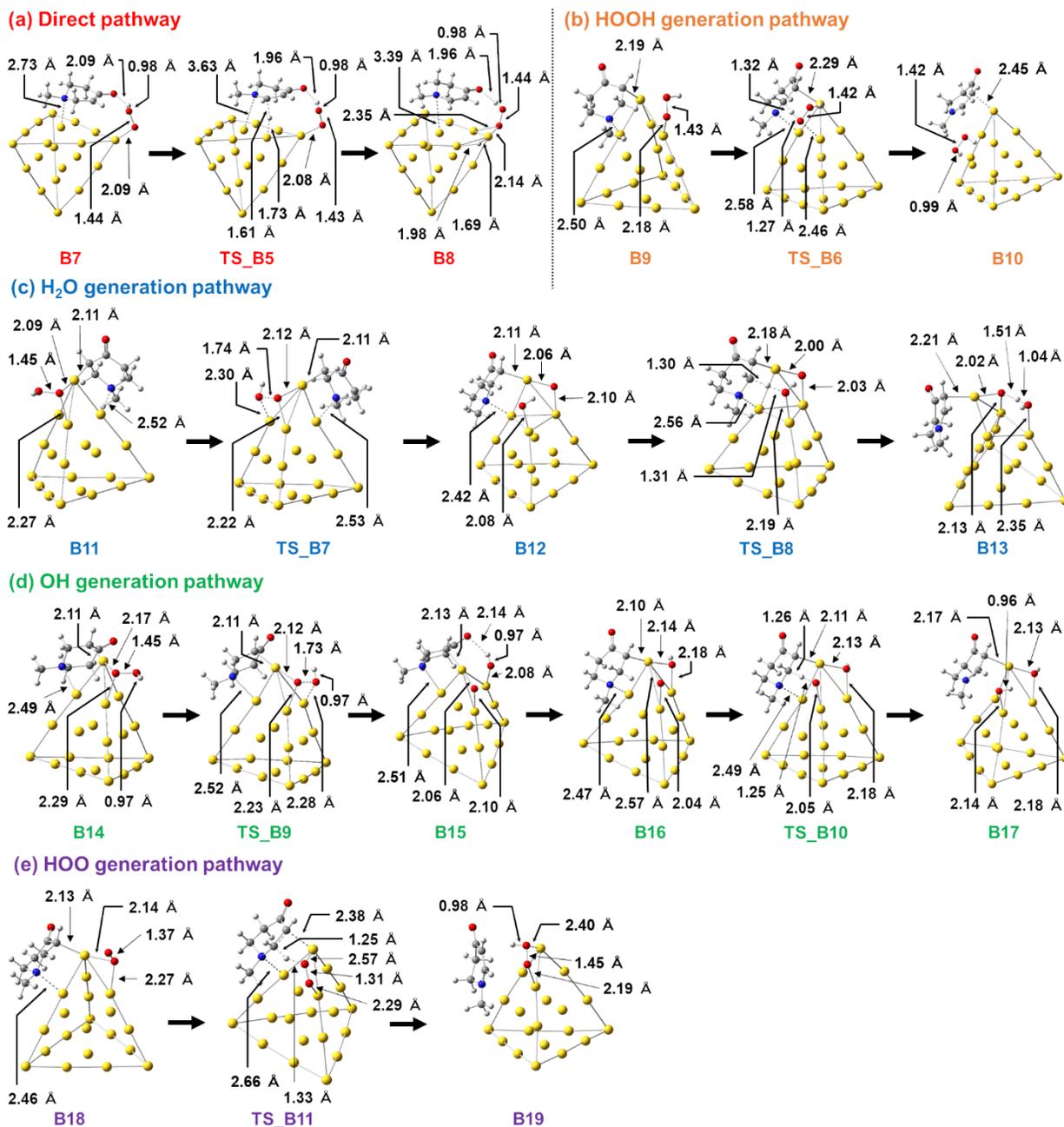
Figure 11. Optimized structures of the reactant, product, and transition states of the second C–H bond cleavage pathway using the Au_{20}^{1-} model. Red: oxygen, blue: nitrogen, gray: carbon, white: hydrogen, yellow: gold.

In the H_2O and OH generation pathways, the conformation of the B4 state became more stable (Figure 11: B11 and B14, respectively) before the O–O bond cleavage of the HOO species. These conformations are more stable than B4 by 3.2 and 3.0 kcal/mol, respectively. The activation energies for the O–O bond cleavage from these states were calculated to be 16.7 and 15.6 kcal/mol, respectively. In the OH generation pathway, the conformation of the intermediate state (B15) became more stable (B16) before C–H^β bond activation. The activation energies for the C–H^β bond cleavage step were calculated to be 24.9 kcal/mol in the H_2O generation pathway and 11.8 kcal/mol in the OH generation pathway. Thus, the C–H^β cleavage step is the rate-determining step of the H_2O generation pathway, whereas the O–O bond cleavage step is the rate-determining step of the OH generation pathway.

In the HOO generation pathway, O_2 is adsorbed on the BR1b site in the reactant state (B18 in Figure 11), although the BR1 site is the most stable adsorption site (cf. Section S3 in the ESI). However, we could not find a transition state that connects to the reactant state with O_2 on the BR1 site. B18 is unstable compared to B4 by 10.9 kcal/mol, and the transition state for C–H^β bond cleavage is 23.6 kcal/mol higher in energy than B18.

In summary, the apparent activation energies (E_{app}) of each pathway were calculated. In the OH generation pathway, the rate-determining step is the O–O bond cleavage step. Thus, E_{app} was calculated from the B14 state, and the barrier was found to be 15.6 kcal/mol (E_{app_OH} in Figure 10). In the H_2O generation pathway, the C–H^β bond cleavage step is the rate-determining step. Thus, E_{app} was calculated from the B12 state, and the barrier was 24.9 kcal/mol (E_{app_H2O} in Figure 10). In the other pathways, the C–H^β activation proceeds through reactive conformations (i.e., B7, B9, and B18), and these states are more unstable than the B4 state, as discussed above. Thus, the apparent activation energies of these pathways should be calculated from the B4 state. The

calculated E_{app} values are 34.3 kcal/mol in the direct pathway (E_{app_direct} in Figure 10), 21.5 kcal/mol in the HOOH generation pathway (E_{app_HOOH} in Figure 10), and 34.5 kcal/mol in the HOO generation pathway (E_{app_HOO} in Figure 10). These results indicate that the OH generation pathway is the most kinetically plausible pathway because it proceeds with the lowest activation barrier (E_{app_OH} = 15.6 kcal/mol) of the five pathways. Additionally, the E_{app} values of the HOOH generation pathway and H_2O generation pathway are also lower than that of the C–H^α cleavage step (E_{aB2} = 29.8 kcal/mol in Figure 5). Thus, these three pathways are plausible routes for the second C–H^β bond cleavage step.

3.6 Total Catalytic Cycle

Because the OH or O species remain on the Au surface after C–H^β bond cleavage via the OH generation pathway and H_2O generation pathway, the total catalytic cycle is not complete. Thus, C–H^α bond cleavage by the remaining O or OH species was also investigated using the Au_{20}^{1-} model (optimized structures along these pathways are shown in Figure S7). The activation energies of these pathways were both calculated to be 17.7 kcal/mol. The reaction energies of C–H^α bond cleavage by the O species and that by the OH species were calculated to be −13.2 and −3.9 kcal/mol, respectively, and both pathways are, thus, exothermic. The total catalytic cycle of the α,β-dehydrogenation of 1-methyl-4-piperidone is summarized in Scheme 4. Because the first C–H^α bond cleavage by the adsorbed O_2 requires the largest activation energy (29.8 kcal/mol) among each reaction step, this step is suggested to be the turnover-limiting step of the total catalytic cycle.

Scheme 4. Total catalytic cycle of the α,β-dehydrogenation of 1-methyl-4-piperidone using the $Au_{20}{}^{1-}$ model.[a]
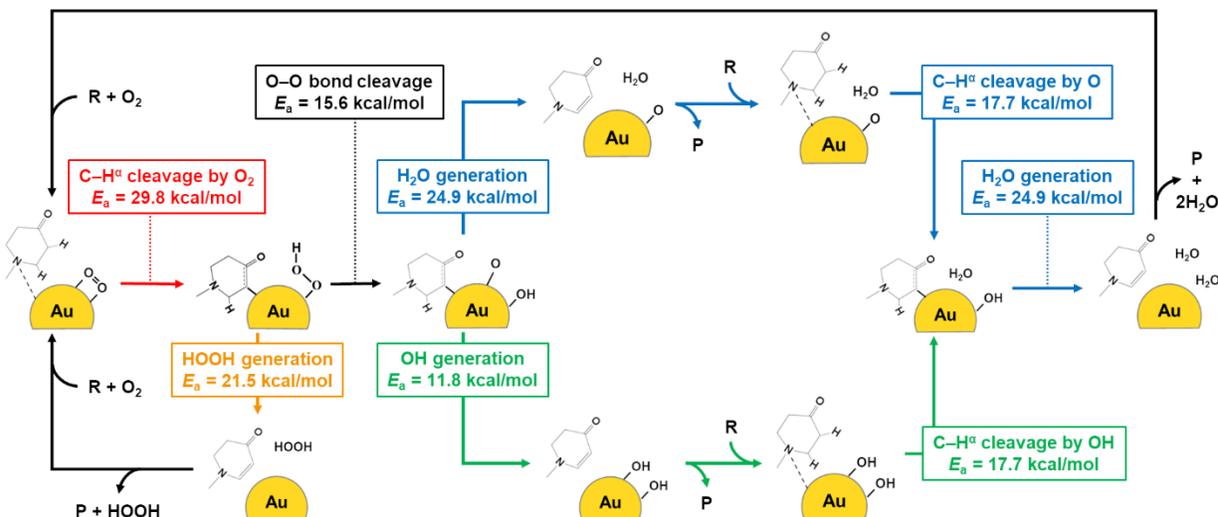
[a]R and P represent 1-methy-4-piperidone (reactant) and the corresponding enaminone (product), respectively.

4. Conclusions

The Au/OMS-2 catalyst is a highly efficient heterogeneous catalyst for the α,β-dehydrogenation of β-*N*-substituted saturated ketones. In this study, the reaction mechanism for the α,β-dehydrogenation of 1-methyl-4-piperidone was investigated mainly by using DFT calculations. The experimental results obtained using Au/OMS-2 suggest that the reaction mechanism at the perimeter region and that at the Au surface co-occur in the Au/OMS-2 catalyst. In a complementary experiment, an Au/C catalyst (Au catalyst without the effect of lattice oxygen of the OMS-2 support) also showed catalytic activity, although only in the presence of gas-phase O_2, indicating the presence of dehydrogenation that occurs only on the Au surface. In the present study, we

focused on the reaction mechanism involving O_2 on the Au surface because the results would be very useful for understanding the general aerobic C–H bond activation mechanism of supported Au catalysts.

In the first C–H bond cleavage step, the H^α of 1-methyl-4-piperidone is abstracted by adsorbed O_2 on the Au cluster. Our DFT calculations suggest that this reaction pathway is more favorable than direct C–H bond activation by Au. Our calculations also suggest that the Au cluster on the OMS-2 support is negatively charged because of charge transfer from the OMS-2 support to the Au cluster. Additionally, adsorbed O_2 on the negatively charged Au cluster is well activated for hydrogen abstraction, which is one of the reasons why the indirect C–H^α bond activation by the adsorbed O_2 is the favorable reaction mechanism. In particular, the degree of O_2 activation increases in more negatively charged Au clusters. According to this trend, the activation barrier for C–H^α bond cleavage by adsorbed O_2 is lower in the more negatively charged Au clusters. This result suggests that the catalytic activity for C–H bond activation could be improved by designing a more negatively charged Au cluster catalyst.

In the second C–H bond cleavage step, the remaining C–H^β bond is activated by adsorbed oxygen species (HOO, OH, and O) generated after C–H^α cleavage by the adsorbed O_2. The activation barrier for the C–H^β cleavage step was lower than that for C–H^α bond cleavage by the adsorbed O_2. Considering that the adsorbed O and OH species can more easily abstract the H^α of another 1-methyl-4-piperidone molecule for subsequent α,β-dehydrogenation reactions, our DFT calculations suggest that the turnover-limiting step of the α,β-dehydrogenation of 1-methyl-4-piperidone is the first C–H^α bond activation by the adsorbed O_2.

FOOT NOTES

†Electronic Supplementary Information.

The following resources are available in the Electronic Supplementary Information: surface structure of OMS-2, adsorption structures of 1-methyl-4-piperidone and O_2 on the Au_{20} models, $C–H^\beta$ bond activation of 1-methyl-4-piperidone in the first C–H bond cleavage step, comparison of calculation settings, definition of the relative potential energies for the second C–H bond cleavage pathways, optimized structures for $C–H^\alpha$ bond activation by the adsorbed O and OH species, Cartesian coordinates of optimized structures throughout the catalytic cycle, and results of control experiments for the α,β-dehydrogenation of 1-methyl-4-piperidone by the Au/OMS-2, Au/Al_2O_3, and Au/C catalysts.

AUTHOR INFORMATION

Corresponding Author

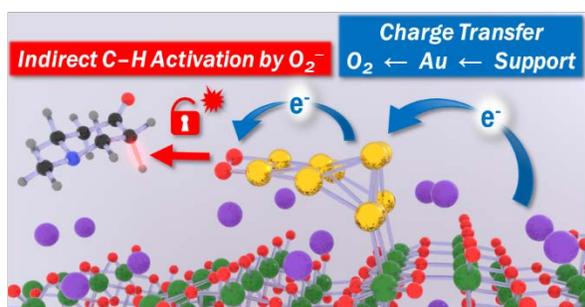*kyama@appchem.t.u-tokyo.ac.jp

*hasegawa@cat.hokudai.ac.jp

CONFLICTS OF INTEREST

There are no conflicts to declare.

・**TOC Graphic**

REFERENCES

1.	G. Negri, C. Kascheres and A. J. Kascheres, *J. Heterocycl. Chem.*, 2004, **41**, 461-491.
2.	A. Z. A. Elassar and A. A. El-Khair, *Tetrahedron*, 2003, **59**, 8463-8480.
3.	A. K. Chattopadhyay and S. Hanessian, *Chem. Commun.*, 2015, **51**, 16437-16449.
4.	A. K. Chattopadhyay and S. Hanessian, *Chem. Commun.*, 2015, **51**, 16450-16467.
5.	T. N. Diao and S. S. Stahl, *J. Am. Chem. Soc.*, 2011, **133**, 14566-14569.
6.	S. S. Stahl and T. Diao, *Compr. Org. Synth.*, 2014, **7**, 178-212.
7.	Z. Z. Zhang, T. Hashiguchi, T. Ishida, A. Hamasaki, T. Honma, H. Ohashi, T. Yokoyama and M. Tokunaga, *Org. Chem. Front.*, 2015, **2**, 654-660.
8.	X. J. Jin, K. Taniguchi, K. Yamaguchi and N. Mizuno, *Chem. Sci.*, 2016, **7**, 5371-5383.
9.	D. Takei, T. Yatabe, X. J. Jin, T. Yabe, N. Mizuno and K. Yamaguchi, *ACS Catal.*, 2020, **10**, 5057-5063.
10.	D. Yoshii, X. J. Jin, T. Yatabe, J. Hasegawa, K. Yamaguchi and N. Mizuno, *Chem. Commun.*, 2016, **52**, 14314-14317.
11.	K. Bobuatong, S. Karanjit, R. Fukuda, M. Ehara and H. Sakurai, *Phys. Chem. Chem. Phys.*, 2012, **14**, 3103-3111.
12.	C. Shang and Z. P. Liu, *J. Am. Chem. Soc.*, 2011, **133**, 9938-9947.

13.   C. R. Chang, Z. Q. Huang and J. Li, *Nano Res.*, 2015, **8**, 3737-3748.
14.   M. Boronat, D. Combita, P. Concepcion, A. Corma, H. Garcia, R. Juarez, S. Laursen and J. D. Lopez-Castro, *J. Phys. Chem. C*, 2012, **116**, 24855-24867.
15.   Y. Ato, A. Hayashi, H. Koga, T. Kawakami, S. Yamanaka and M. Okumura, *Chem. Phys. Lett.*, 2019, **724**, 115-121.
16.   M. Okumura, Y. Kitagawa, T. Kawakami and M. Haruta, *Chem. Phys. Lett.*, 2008, **459**, 133-136.
17.   K. Sakata, Y. Ato, K. Tada, H. Koga, S. Yamanaka, T. Kawakami, T. Saito and M. Okumura, *Chem. Lett.*, 2016, **45**, 344-346.
18.   J. Engel, S. Francis and A. Roldan, *Phys. Chem. Chem. Phys.*, 2019, **21**, 19011-19025.
19.   H. J. Freund and G. Pacchioni, *Chem. Soc. Rev.*, 2008, **37**, 2224-2242.
20.   G. Pacchioni and H. J. Freund, *Chem. Soc. Rev.*, 2018, **47**, 8474-8502.
21.   M. Boronat, P. Concepcion and A. Corma, *J. Phys. Chem. C*, 2009, **113**, 16772-16784.
22.   D. Y. Tang and C. W. Hu, *J. Phys. Chem. Lett.*, 2011, **2**, 2972-2977.
23.   B. Yoon, H. Hakkinen, U. Landman, A. S. Worz, J. M. Antonietti, S. Abbet, K. Judai and U. Heiz, *Science*, 2005, **307**, 403-407.
24.   A. Roldan, J. M. Ricart, F. Illas and G. Pacchioni, *Phys. Chem. Chem. Phys.*, 2010, **12**, 10723-10729.
25.   M. Gao, D. Horita, Y. Ono, A. Lyalin, S. Maeda and T. Taketsugu, *J. Phys. Chem. C*, 2017, **121**, 2661-2668.
26.   B. Yoon, H. Hakkinen and U. Landman, *J. Phys. Chem. A*, 2003, **107**, 4066-4071.
27.   M. Okumura, Y. Kitagawa, M. Haruta and K. Yamaguchi, *Chem. Phys. Lett.*, 2001, **346**, 163-168.
28.   D. A. Tompsett, S. C. Parker and M. S. Islam, *J. Mater. Chem. A*, 2014, **2**, 15509-15518.
29.   T. Gao, M. Glerup, F. Krumeich, R. Nesper, H. Fjellvag and P. Norby, *J. Phys. Chem. C*, 2008, **112**, 13134-13140.
30.   V. Blum, R. Gehrke, F. Hanke, P. Havu, V. Havu, X. G. Ren, K. Reuter and M. Scheffler, *Comput. Phys. Commun.*, 2009, **180**, 2175-2196.
31.   J. P. Perdew, K. Burke and M. Ernzerhof, *Phys. Rev. Lett.*, 1996, **77**, 3865-3868.
32.   E. Cockayne and L. Li, *Chem. Phys. Lett.*, 2012, **544**, 53-58.
33.   J. Li, X. Li, H. J. Zhai and L. S. Wang, *Science*, 2003, **299**, 864-867.
34.   G. W. T. M. J. Frisch, H. B. Schlegel, G. E. Scuseria, M. A. Robb, J. R. Cheeseman, G. Scalmani, V. Barone, G. A. Petersson, H. Nakatsuji, X. Li, M. Caricato, A. Marenich, J. Bloino, B. G. Janesko, R. Gomperts, B. Mennucci, H. P. Hratchian, J. V. Ortiz, A. F. Izmaylov, J. L. Sonnenberg, D. Williams-Young, F. Ding, F. Lipparini, F. Egidi, J. Goings, B. Peng, A. Petrone, T. Henderson, D. Ranasinghe, V. G. Zakrzewski, J. Gao, N. Rega, G. Zheng, W. Liang, M. Hada, M. Ehara, K. Toyota, R. Fukuda, J. Hasegawa, M. Ishida, T. Nakajima, Y. Honda, O. Kitao, H. Nakai, T. Vreven, K. Throssell, J. A. Montgomery, Jr., J. E. Peralta, F. Ogliaro, M. Bearpark, J. J. Heyd, E. Brothers, K. N. Kudin, V. N. Staroverov, T. Keith, R. Kobayashi, J. Normand, K. Raghavachari, A. Rendell, J. C. Burant, S. S. Iyengar, J. Tomasi, M. Cossi, J. M. Millam, M. Klene, C. Adamo, R. Cammi, J. W. Ochterski, R. L. Martin, K. Morokuma, O. Farkas, J. B. Foresman, and D. J. Fox, *Gaussian 09, revision B.01*, 2016, **Gaussian, Inc., Wallingford, CT**.
35.   Y. Zhao and D. G. Truhlar, *Theor. Chem. Acc.*, 2008, **120**, 215-241.

36. D. Andrae, U. Haussermann, M. Dolg, H. Stoll and H. Preuss, *Theoret. Chim. Acta*, 1990, **77**, 123-141.
37. W. J. Hehre, R. Ditchfield and J. A. Pople, *J. Chem. Phys.*, 1972, **56**, 2257-2261.
38. F. L. Hirshfeld, *Theoret. Chim. Acta*, 1977, **44**, 129-138.
39. I. X. Green, W. J. Tang, M. Neurock and J. T. Yates, *Science*, 2011, **333**, 736-739.
40. L. C. Liu and A. Corma, *Chem. Rev.*, 2018, **118**, 4981-5079.
41. T. Ishida, H. Koga, M. Okumura and M. Haruta, *Chem. Rec.*, 2016, **16**, 2278-2293.
42. Z. P. Liu, P. Hu and A. Alavi, *J. Am. Chem. Soc.*, 2002, **124**, 14770-14779.
43. H. Koga, K. Tada and M. Okumura, *Chem. Phys. Lett.*, 2014, **610**, 76-81.
44. M. Okumura, M. Haruta, Y. Kitagawa and K. Yamaguchi, *Gold Bull.*, 2007, **40**, 40-44.